A comparative study on the performance of a novel triangular solar air collector with tilted transparent cover plate

Yan Jiang [a, b], Huan Zhang [a, b], Yaran Wang [a, b, *], Shijun You [a, b], Zhangxiang Wu [a, b], Man Fan [a], Liwen Wang [c], Shen Wei [d]

[a] School of Environmental Science and Engineering, Tianjin University, Haihe Education Area, Jinnan District, Tianjin 300350, PR China

[b] Tianjin Key Lab of Biomass/Wastes Utilization, Tianjin 300350, PR China

[c] Tianjin University Research Institute of Architectural Design and Urban Planning Co., Ltd, Nankai District, Tianjin 300072, PR China

[d] The Bartlett School of Construction and Project Management, University College London (UCL), 1-19 Torrington Place, London WC1E 7HB, United Kingdom

Abstract

The application of solar air collector (SAC) in rural residence is beneficial to the realization of clean heating in rural areas and improvement of the thermal comfort in the rural residence, but the available covered area for the SAC on the south wall of rural residence is limited. In this research, a novel triangular solar air collector (TSAC) with a tilted transparent cover plate is proposed. With the same south wall covered area, the TSAC can receive more solar irradiance, which improves the heat collecting power. A mathematical model of the TSAC is established. Experiments are conducted to validate the model. The performances of the TSAC and the flat plate solar air collector (FSAC) with the same perforated corrugated absorber (PCA) are compared and analyzed under different operation conditions. Results indicate that: (1) The collecting power per unit south wall covered area (CPUWA) of the TSAC with the 60° transparent cover plate (TSAC 60°) is 100 ~ 130 W/m^2 higher than that of the FSAC. (2) The thermal efficiency of the TSAC increases faster with the increase of solar irradiance, due to the large area of transparent cover plate. (3) During the heating period, the heat collection capacity and solar fraction of the TSAC 60° are 24.3% and 11.7% higher than those of the FSAC, respectively.

Keywords:

solar air heating; solar air collector; heat transfer model; thermal performance; solar fraction

Nomenclature	
A	surface area (m^2)
A_{wall}	south wall covered area of collector (m^2)
c_{p}	specific heat capacitance (J/(kg·K))
d	thickness (m)
h_{conv}	convective heat transfer coefficient (W/(m^2·K))
h_{rad}	radiant heat transfer coefficient (W/(m^2·K))
I_{b}	beam solar irradiance (W/m^2)
I_{d}	diffuse solar irradiance (W/m^2)
I_{g}	global solar irradiance (W/m^2)
M	mass (kg)
m	mass flow rate (the product of the flow rate and density) (kg/s)
P	porosity factor (-)
Q_{c}	heat collecting capacity (J)
Q_{h}	heat loos of the rural residence (J)
Q_{u}	net heat gain (W)
Q_{wall}	heat collecting power of per unit south wall covered area (W/m^2)
q_{conv}	convective heat transfer (W)
q_{rad}	radiant heat transfer (W)
D	aperture (m)
S_{b}	beam solar irradiance absorbed (W)
S_{d}	diffuse solar irradiance absorbed (W)
T	temperature (°C)
u	the velocity in the x direction (m/s)
V	volume (m^3)
V_{air}	flow rate (m^3/h)
v_{in}	inlet air velocity (m/s)
v_{env}	wind speed (m/s)
Subscripts	

ab	absorber
air	recirculated air
env	environment
ho	insulation housing
in	inlet
out	outlet
tcp	transparent cover plate
Greek symbols	
α	absorptivity (-)
β	inclination angle (°)
ε	emissivity (-)
η_t	thermal efficiency (%)
λ	thermal conductivity coefficient (W/(m·K))
τ	time (s)
τ_t	transmittance of transparent cover plate (-)
Abbreviations	
TSAC	triangular solar air collector
FSAC	flat plate solar air collector
CPUWA	collecting power per unit south wall covered area
PCAs	perforated corrugated absorbers

1. Introduction

In rural areas of northern China, the traditional coal-fired heating is gradually replaced by clean energy to reduce the emissions of pollutants in winter (Deng et al., 2021). The solar air collector (SAC) is widely adopted in rural residence as an auxiliary heating measure (Hu et al., 2018), due to its advantages in simple-structure, low-costs and durability. As the air is taken as the heat transfer fluid, the risks of freezing and leakage are avoided (Zhang et al., 2021). The SAC is easy to integrate with the wall to improve the insulation performance of the rural residence (Zhao et al., 2020).

Recent studies on the SAC were mainly focused on improving the thermal performance by absorber surface modifications, multi-channel of air, porous absorber and air jet impingement absorber (Vengadesan and Senthil, 2020; Kumar et al., 2019). Li et al. (2017) compared the heat transfer coefficient of the sinusoidal corrugated absorber, protrusion absorber, sinusoidal corrugated and protrusion absorber. Results show that the heat transfer coefficient increases with the increase of the absorber surface roughness. Singh et la. (2021) proposed the absorber with small cylindrical tubes, which significantly increased the exhaust air temperature of SAC compared to the flat plate type absorber. Tuncer et al. (2020) designed a quadruple-pass solar air collector, and the mean thermal efficiency is within the range of 71.63 ~ 80.66%. Razak et al. (2019) presented a novel porous absorber with compact cross-matrix absorber incorporating metal hollow square-tube absorbers, and the effect of square-tube arrangement on collector performance was studied. Singh et al. (2020) proposed a double-corrugated plate SAC, of which the thermal performance improved by circulating jet impingement. Shetty et al. (2021) designed a SAC with circular perforated absorber, the laminar viscous layer was eliminated by jet impingement and the thermo-hydraulic performance was improved. In the above measures, porous absorber and air jet impingement absorber were considered to be effective approaches to improve the thermal performance of SAC.

In addition, Kenna et al. (1983) proposed the transpired SAC, which has the advantages in both porous absorber and air jet impingement absorber. The perforated absorber of the transpired SAC significantly enhances the convective heat transfer and increases the collector efficiency (Gao et al., 2020). The transpired SAC can be classified as the unglazed transpired collectors (UTC) and the glazed transpired collectors (GTC) (Kumar, 2020). The GTC is considered to be prospective in colder regions (Saxena et al., 2015). Gao et al. (2020) proposed a GTC with non-uniform perforated corrugated absorber (PCA), and the thermal efficiency is 20% higher than the traditional collector. Li et al. (2016) designed a slit-like perforated absorber GTC, and the effect of key parameters on the net heat gain were studied. Zhang et al. (2018) presented a SAC combining the GTC and corrugated packing. The effective efficiency can reach 67.83%, when the air velocity in the collectors is 1.14 m/s. Zhou et al. (2020) designed a GTC and hollow ventilated interior wall coupling system suitable for residential buildings on Tibetan Plateau, and the coupling system could provide thermal energy for residential buildings at nighttime. Zhang et al. (2016) applied the GTC to rural areas of northeast China, and the results showed that the GTC can effectively improve the indoor thermal comfort and reduce indoor environmental pollution in cold areas. Hence, the heat transfer efficiency of the GTC is higher and it is considered as a suitable measure for clean heating in rural residence.

Studies on the modeling and simulation are essential for performance enhancement of the SAC (Saxena et al., 2020a). Badescu et al. (2019) established a one-node model to analyze the performance of SAC. The instantaneous indicators and variability factors were defined to represent the deviations between the instantaneous and the global values of efficiency and performance coefficient. Sun et al (2016) proposed a mathematical model of the coupled momentum and energy for the SAC. The finite-difference approach is adopted to solve the model. Demou and Grigoriadis (2018) established a one-dimensional model for the SAC, considering the meteorological parameters, collector materials, geometric parameters and orientation. They calculated the operating temperatures and heat transfer rates of the collector using the one-dimensional model during a whole heating period. Lin et al. (2020) established the mathematical model of SAC with corrugated absorber. The effects of absorber surface absorptance, opening angle, collector geometry parameters on the performances were analyzed. Zheng et al. (2016) proposed a GTC with the PCA, and a multivariable one-dimensional mathematical model was established based on the energy balance equation, to study the influences of the key parameters on the collector performance.

Previous studies mainly focus on the performance improvement of the flat plate solar air collector (FSAC). However, the area available for covering the SAC on the south wall is limited, receiving more solar irradiance with limited south wall area is the key to the application of the SAC in rural residence. In this paper, a novel triangular solar air collector (TSAC) combining the GTC and the PCA is proposed. In the proposed TSAC, the tilted transparent cover plate is adopted to receive more solar irradiance. Compared with the FSAC installed at the same tilt, the TSAC has larger heat exchange area to increase the thermal performance and is feasible to be integrated with the wall to improve the insulation performance of the rural residence. The dynamic model of TSAC is established and validated by experiments. The collecting power per unit south wall covered area (CPUWA), thermal efficiency, heat collecting capacity of the heating period and solar fraction of the TSAC and FSAC with the same PCA are compared under different conditions. The main contributions of this study include three parts: (1) A novel TSAC with tilted transparent cover plate was proposed; (2) The dynamic mathematical model was established; (3) The novel TSAC and conventional FSAC were compared and studied.

2. Methods

2.1 The TSAC structure

Structure of the TSAC with PCAs is shown in Fig. 1. The TSAC is orientated to south, and the inclination angle of tilted glass cover is 60° which can penetrate more solar irradiance. The PCAs can enhance the turbulent intensity and improve the heat transfer efficiency as the laminar boundary on its surface is destructed by porosity and corrugated structure. The porosity factor of the PCAs is 0.085, and the aperture is 4 mm. To improve the utilization of solar energy, the PCAs are coated with black chromium deposition and the absorption could reach 0.92. In addition, the PCAs are divided into three parts, the inclination angles are 30°, 120°, and 52° to ensure that the PCAs can receive solar irradiation from sunrise to sunset, and the three parts of PCAs don't block each other. When the TSAC is working, the PCAs will be heated by the solar irradiance. The recirculated air will be drawn from the indoor into the TSAC, which goes through the PCAs and exchanges heat with it. The heated air finally returns the room through the air outlet. To minimize the heat loss of TSAC to the environment, the sides, backs and undersides of the TSAC were fitted with insulation material. The geometric and physical parameters of the TSAC were listed in Table 1.

Table 1 The geometric and physical parameters of the TSAC.

TSAC	Section size: 2.4×2.1×1.2 (m×m×m), width: 0.7 (m)
Inlet duct	Section size: 0.15×0.4 (m×m), length: 0.6 (m)
Outlet duct	Section size: 0.2×0.2 (m×m), length: 0.6 (m)
Transparent cover plate	Materials: Polycarbonate;
	Size: 2.4×0.7×0.004 (m×m×m)

	Physical parameter: λ_{tcp}=0.2 (W/(m·K)); τ_t=0.82; α_{tcp}=0.1; ε_{tcp}=0.67
Perforated corrugated absorber	Materials: Stainless steel
	Size: 0.65/0.80/1.39×0.7×0.00015 (m×m×m);
	Physical parameter: λ_{ab}=14.8 (W/(m·K)); α_{ab}=0.92; ε_{ab}=0.2;
Insulation housing	Materials: Polystyrene board and galvanized sheet
	Physical parameter: λ_{ho}=0.028 (W/(m·K)); ε_{ho}=0.1

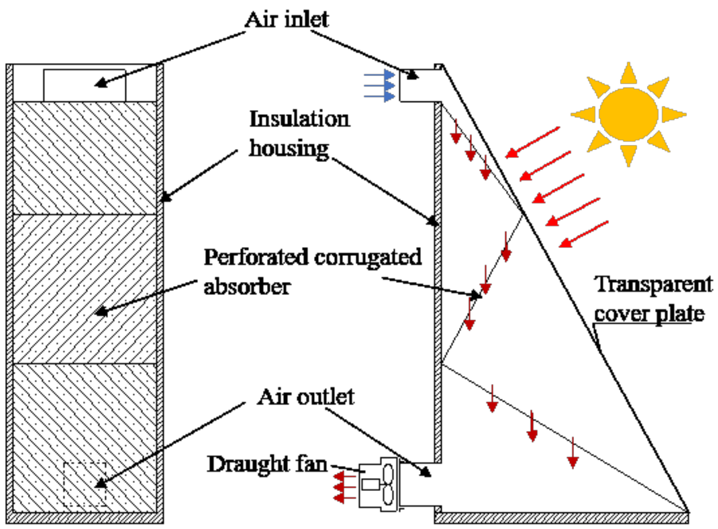

Fig. 1. Structure of the TSAC.

2.2 Assumptions

The following assumptions are considered to establish the mathematical model of the TSAC:

(1) The temperature and pressure have little change in the TSAC, and the density of recirculating air is constant;

(2) The recirculating air velocity is evenly distributed on the TSAC cross sections;

(3) The thermal properties of the recirculating air, insulation housing, PCA, and transparent cover plate are temperature independent;

(4) The heat losses between the insulation housing and the external environment are ignored.

2.3 Mathematical model

A one-dimensional model is established along the height direction of TSAC. The energy conservation equations for insulation housing, transparent cover plate, PCA, and four parts of recirculation air separated by PCA are considered. The heat transfer includes the internal heat conduction of TSAC solid parts (including insulation housing, transparent cover plate, PCA), the irradiance heat transfer between the TSAC solid parts, the convection heat transfer of recirculating air, the convection heat transfer between recirculating air and TSAC solid parts, and the convection and irradiance heat transfer between transparent cover plate and the external environment. These heat transfer processes are shown in Fig. 2. The diffusion terms of the recirculation air conservation equations along the flow direction are ignored.

Energy conservation equation for the transparent cover plate can be expressed as:

$$M_{\mathrm{tcp}} c_{\mathrm{p.tcp}} \frac{\partial T_{\mathrm{tcp}}}{\partial \tau} = V_{\mathrm{tcp}} \lambda_{\mathrm{tcp}} \frac{\partial^2 T_{\mathrm{tcp}}}{\partial x^2} + s_{\mathrm{b.tcp}} + s_{\mathrm{d.tcp}} + q_{\mathrm{conv.tcp\text{-}env}} + q_{\mathrm{conv.tcp\text{-}air}} + q_{\mathrm{rad.tcp\text{-}env}} + q_{\mathrm{rad.tcp\text{-}ab}} + q_{\mathrm{rad.tcp\text{-}ho}} \quad (1)$$

Energy conservation equation for the PCA can be formulated as:

$$M_{\mathrm{ab}} c_{\mathrm{p.ab}} \frac{\partial T_{\mathrm{ab}}}{\partial \tau} = V_{\mathrm{ab}} \lambda_{\mathrm{ab}} \frac{\partial^2 T_{\mathrm{ab}}}{\partial x^2} + s_{\mathrm{b.ab}} + s_{\mathrm{d.ab}} + q_{\mathrm{conv.ab\text{-}air}} + q_{\mathrm{conv.hole}} + q_{\mathrm{rad.ab\text{-}tcp}} + q_{\mathrm{rad.ab\text{-}ho}} + q_{\mathrm{rad.ab\text{-}ab}} \quad (2)$$

Energy conservation equation for the insulation housing can be derived as:

$$M_{\mathrm{ho}} c_{\mathrm{p.ho}} \frac{\partial T_{\mathrm{ho}}}{\partial \tau} = V_{\mathrm{ho}} \lambda_{\mathrm{ho}} \frac{\partial^2 T_{\mathrm{ho}}}{\partial x^2} + q_{\mathrm{conv.ho\text{-}air}} + q_{\mathrm{rad.ho\text{-}tcp}} + q_{\mathrm{rad.ho\text{-}ab}} + q_{\mathrm{rad.ho\text{-}ho}} \quad (3)$$

Energy conservation equation for the recirculation air can be written as:

$$M_{\mathrm{air}} c_{\mathrm{p.air}} \frac{\partial T_{\mathrm{air}}}{\partial \tau} + M_{\mathrm{air}} c_{\mathrm{p.air}} \frac{\partial (u_{\mathrm{air}} T_{\mathrm{air}})}{\partial x} = q_{\mathrm{conv.ho\text{-}air}} + q_{\mathrm{conv.hole}} + q_{\mathrm{conv.tcp\text{-}air}} + q_{\mathrm{conv.ab\text{-}air}} \quad (4)$$

The irradiance heat transfer between the TSAC solid parts is calculated using the Kirchhoff's law of irradiance, and the heat transfer between other parts is calculated as:

$$q_{\text{conv.tcp-env}} = h_{\text{conv.tcp-env}} A_{\text{tcp}} \left(T_{\text{tcp}} - T_{\text{env}} \right) \tag{5}$$

$$q_{\text{conv.tcp-air}} = h_{\text{conv.tcp-air}} A_{\text{tcp}} \left(T_{\text{tcp}} - T_{\text{air}} \right) \tag{6}$$

$$q_{\text{rad.tcp-env}} = h_{\text{rad.tcp-env}} A_{\text{tcp}} \left(T_{\text{tcp}} - \sqrt[4]{\frac{1+\cos\beta_{\text{tcp}}}{2}\varepsilon_{\text{sky}} + \frac{1-\cos\beta_{\text{tcp}}}{2}} T_{\text{env}} \right) \tag{7}$$

$$q_{\text{conv.ab-air}} = h_{\text{conv.ab-air}} A_{\text{ab}} \left(1-P\right)\left(T_{\text{ab}} - T_{\text{air}} \right) \tag{8}$$

$$q_{\text{conv.hole}} = h_{\text{conv.hole}} A_{\text{ab}} \frac{4 d_{\text{ab}} P}{D}\left(T_{\text{ab}} - T_{\text{air}} \right) \tag{9}$$

$$q_{\text{conv.ho-air}} = h_{\text{conv.ho-air}} A_{\text{ho}} \left(T_{\text{ho}} - T_{\text{air}} \right) \tag{10}$$

The heat transfer coefficients between the transparent cover plate and environment, the $h_{\text{conv.tcp-env}}$ and $h_{\text{rad.tcp-env}}$ are proposed by Watmuff et al. (1977) and Kumar et al. (2009). The convective heat transfer coefficients $h_{\text{conv.tcp-air}}$, $h_{\text{conv.ab-air}}$ and $h_{\text{conv.ho-air}}$ are proposed by Leon and Kumar (2007). The convective heat transfer coefficient of recirculating air through the PCA, $h_{\text{conv.hole}}$ is proposed by Vandecker et al. (2001).

The boundary conditions of the mathematical model are $T_{\text{air}}\left(x,\tau\right)\big|_{x=0} = T_{\text{in}}\left(\tau\right)$, $m_{\text{air}}\left(x,\tau\right)\big|_{x=0} = m_{\text{in}}\left(\tau\right)$, and the variations of environmental temperature T_{env}, wind speed v_{env}, solar irradiance I_{g} with time are considered. The initial conditions of the mathematical model are listed below:

$$T_{\text{air}}\left(x,\tau\right)\big|_{\tau=0} = T_{\text{tcp}}\left(x,\tau\right)\big|_{\tau=0} = T_{\text{ab}}\left(x,\tau\right)\big|_{\tau=0} = T_{\text{ho}}\left(x,\tau\right)\big|_{\tau=0} = T_{\text{env}}\big|_{\tau=0}.$$

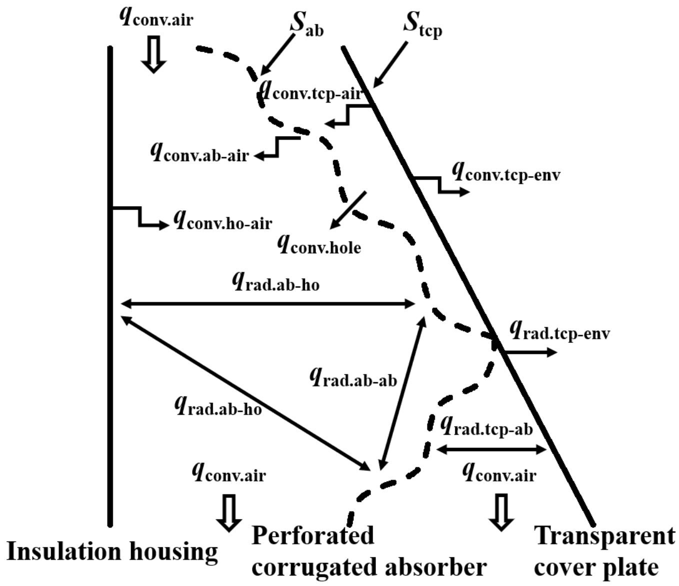

Fig. 2. The heat transfer relationships of TSAC.

2.4 Numerical method

The temperatures of TSAC solid parts are solved iteratively. The diffusion terms of the energy conservation equation are discretized by the central difference scheme. The first-order upwind scheme is adopted to discretize the convective terms. The unsteady terms are discretized by the fourth-order Runge-Kutta integration. The flowchart of the numerical method is shown in Fig. 3.

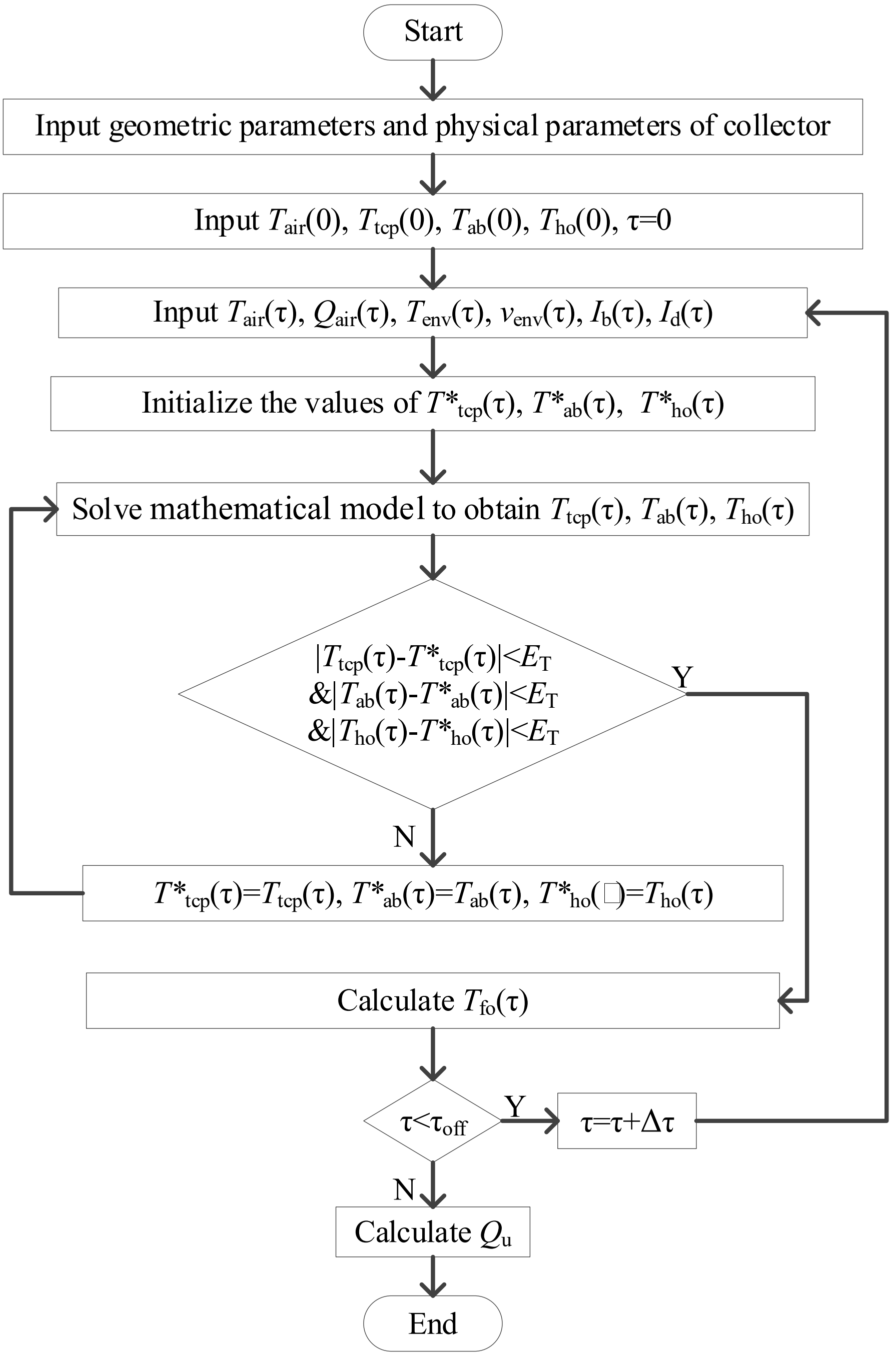

Fig. 3 Flowchart of the numerical method.

2.5 Evaluation indices

The south wall covered area and material of the TSAC and FSAC compared are the same. The only difference is that the transparent cover plate of the TSAC is tilted. Furthermore, in order to study the effect of the inclination angle of the transparent cover plate on the performance of the TSAC, the inclination angle of 60° (TSAC 60°) and 75° (TSAC 75°) are compared.

To evaluate the performance of the three collectors, the thermal efficiency η_t (Fan et al., 2020), heat collecting capacity Q_c (Yu et al., 2020), solar fraction SF (Acuna et al., 2017) and the CPUWA Q_{wall} are defined as follows.

$$\eta_t = \frac{Q_u}{A_{tcp} \times I_g} = \frac{\dot{m}_{air} c_{p.air} \left(T_{out} - T_{in}\right)}{A_{tcp} \times I_g} \times 100\% \tag{11}$$

$$Q_c = \int_{\tau_0}^{\tau_{off}} \dot{m}_{air} c_{p.air} \left(T_{out} - T_{in}\right) d\tau \tag{12}$$

$$SF = \frac{\int_{\tau_0}^{\tau_{off}} \dot{m}_{air} c_{p.air} \left(T_{out} - T_{in}\right) d\tau}{Q_h} \tag{13}$$

$$Q_{wall} = \frac{\dot{m}_{air} c_{p.air} \left(T_{out} - T_{in}\right)}{A_{wall}} \tag{14}$$

The heat loss of the rural residence (Q_h) is simulated by EnergyPlus. Geometric and physical parameters of the rural residence are listed in Table 2.

Table 2 Geometric and physical parameters of the rural residence.

Rural residence	Size: 3×4.7×4.7 (m×m×m)
Window	Heat transfer coefficient: 0.35 (W/(m^2·K)) Window-wall ratio: 0.3 Position: The south wall of rural residence
Door	Heat transfer coefficient: 2.8 (W/(m^2·K)) Size: 2.3×1 (m×m) Position: The south wall of rural residence
	Heat transfer coefficient: 2.5 (W/(m2·K))

3. Model validation

3.1 Experimental system

An experimental system was setup to test the performance of the proposed TSAC and validate the mathematical model. The photograph of the TSAC experimental rig is depicted in Fig. 4. The experimental system mainly includes the TSAC, a thermostatic air tank and a draught fan. The air inlet and outlet of the TSAC were extended into the thermostat air tank. The draught fan was installed at the air outlet and the maximum air flow rate was 980 m^3/h. The air flow was controlled by adjusting the fan speed.

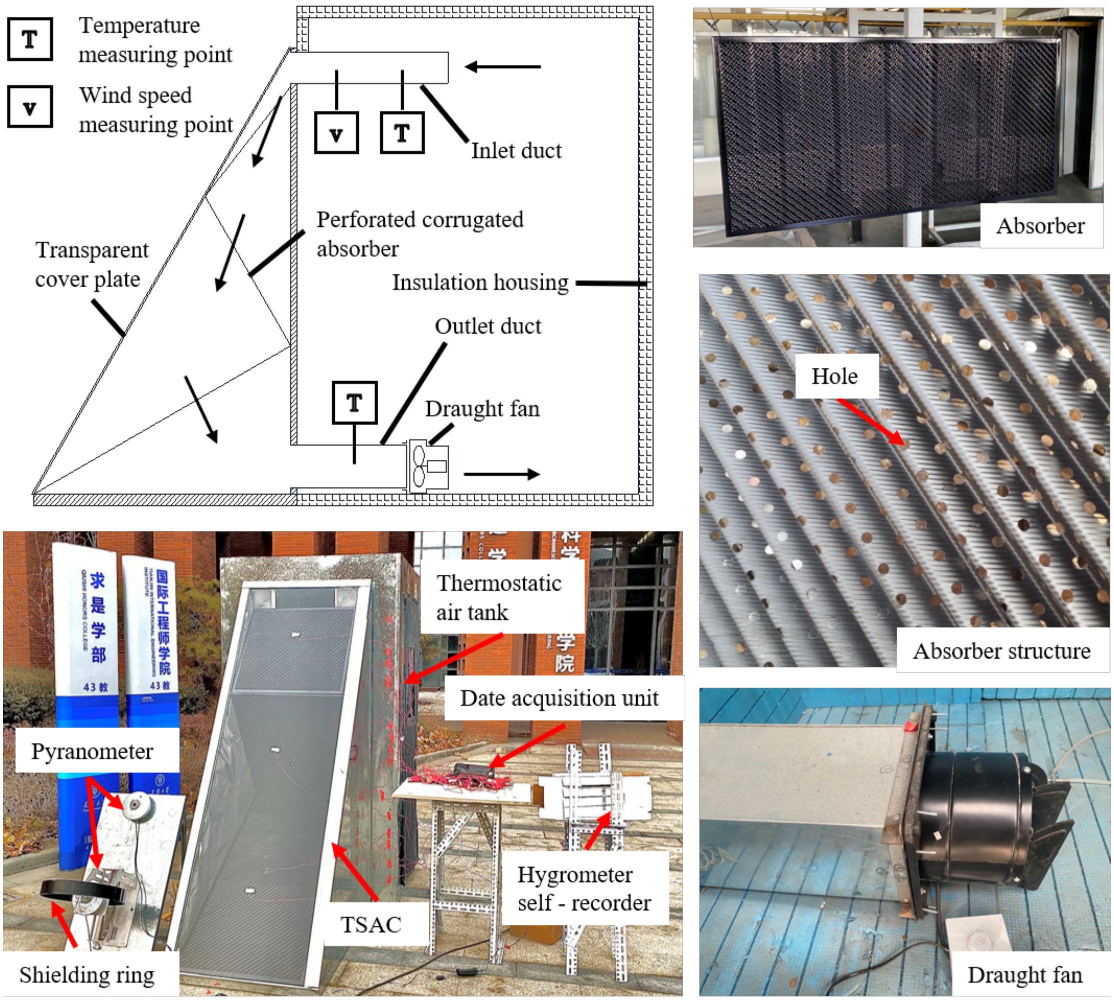

Fig. 4. Sketch and photograph of experimental rig for TSAC

During the test, the inlet temperature T_{in}, outlet temperature T_{out} and the inlet air velocity v_{in} of the TSAC were monitored. The environmental temperature T_{env}, wind speed v_{env}, global solar irradiance I_g and diffuse solar irradiance I_d were monitored every 5 seconds. The pyranometer had the same inclination angle as the TSAC, and the diffuse irradiance pyranometer was fitted with a shielding ring. The monitoring instrument of the environmental temperature was placed in a white louver box to avoid the effect of solar irradiance on the measurement accuracy. After changing the test condition, the data were recorded as the collector operates at least 20 minutes. The ranges and uncertainties of measuring instruments were listed in Table 3. The uncertainty of the recirculation air net heat gain Q_u was calculated according to the equation proposed by Kashif et al. (2020), and it could be converted into Eq. (15).

$$E_{Q_u} = \sqrt{\left(\Delta v_{\text{in}} \frac{\partial Q_u}{\partial v_{\text{in}}}\right)^2 + \left(\Delta T_{\text{in}} \frac{\partial Q_u}{\partial T_{\text{in}}}\right)^2 + \left(\Delta T_{\text{out}} \frac{\partial Q_u}{\partial T_{\text{out}}}\right)^2} \tag{15}$$

where E_{Qu}, Δv_{in}, ΔT_{in}, ΔT_{out} were the uncertainty of the recirculation air net heat gain, inlet air velocity, inlet temperature and outlet temperature, respectively. During the test, the average uncertainty of the recirculation air net heat gain was 12.3%.

Table 3 Ranges and uncertainties of measuring instruments.

Parameters	Instruments	Ranges	Uncertainties
T_{in}, T_{out}	T-type sheathed thermocouple	-50 ~ 150 °C	±0.5 °C
v_{in}	Testo-405i hotwire probe	0 ~ 30 m/s	±0.1 m/s
T_{env}	Hygrometer self - recorder	-35 ~ 150 °C	±0.5 °C
v_{env}	Testo-405i hotwire probe	0 ~ 30 m/s	±0.1 m/s
I_g, I_d	TBQ-2-B pyranometer	0 ~ 1400 W/m^2	±2%

3.2 Experimental results and model validation

During the test, the inlet air temperature and flow rate were varied. The range of inlet air temperature T_{in} and flow rate V_{air} were maintained at 12 ~ 18 °C and 130 ~280 m^3/h, respectively. Comparison between the tested and predicted values of the outlet temperature T_{out} and the recirculation air net heat gain Q_{u} at different inlet conditions were depicted in Fig. 5. When the flow rate was maintained constant at 201.7 m^3/s, the average relative errors of the outlet temperature and the net heat gain were 3.1% and 7.1%, the maximum relative errors were 4.6% and 10.8%. When the inlet air temperature was maintained constant at 14.5 °C, the average relative errors of the outlet temperature and the net heat gain were 2.7% and 5.6%, the maximum relative errors were 6.0% and 10.8%. The tested and predicted results show satisfied agreements, which indicates the reliability of the proposed mathematical model.

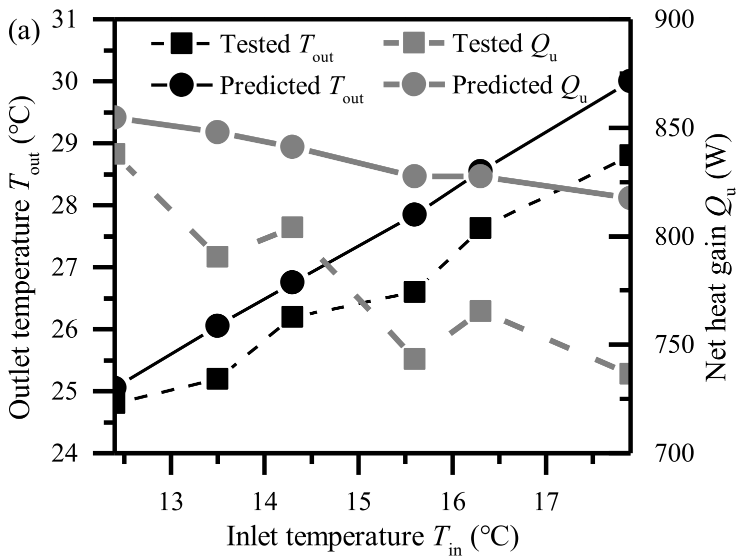

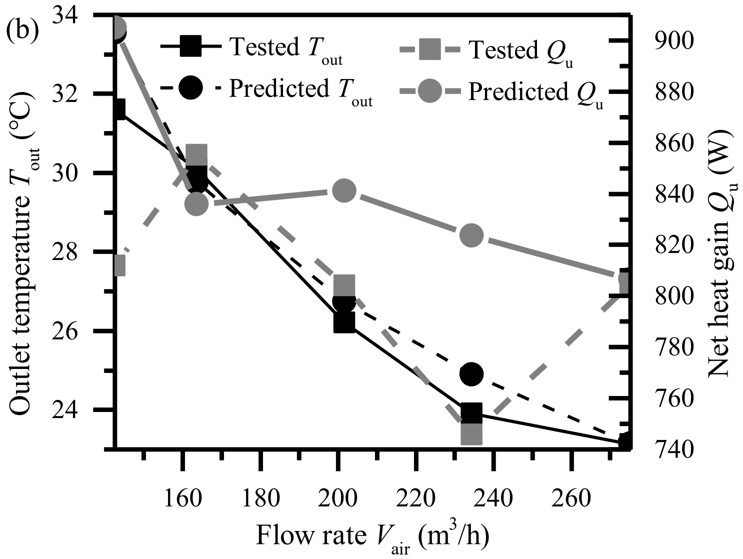

Fig. 5. Comparison between tested and predicted results at different (a) inlet air temperature, and (b) flow rate.

4. Result and discussion

The effect of operation and environmental parameters on the performances of the TSAC 60°, TSAC 75° and FSAC are compared using the mathematical model. And the following parameters were maintained constant: T_{in} = 14.5 °C, V_{air} = 144 m^3/h, T_{env} =1.85 °C, v_{env} = 2 m/s, I_b = 600 W/m^2, I_d =150 W/m^2.

4.1 Effects of operation parameters

Effects of the inlet air temperature on the performances of the three collectors are compared as shown in Fig. 6. With the increase of the inlet air temperature, the recirculation air temperature in the collector and the outlet increases. Therefore, the convection and radiant heat loss to the environment through the transparent cover plate increase, while the thermal efficiency decreases. The inlet temperature is linearly related to the outlet temperature and thermal efficiency. Thermal efficiency of the

TSAC decreases faster as the area of transparent cover plate is large, which can be compensated by using the double transparent cover plate. The thermal efficiency of the FSAC is 0.6% higher than that of TSAC. Due to the increased area of transparent cover plate, the average outlet temperature of TSAC 60° is 2.2 ℃ and 3.9 ℃ higher than that of TSAC 75° and FSAC. The CUPWA decreases as the thermal efficiency descends. The average CPUWA of TSAC 60° is 71.9 W/m^2 and 127.2 W/m^2 higher than that of the TSAC 75° and FSAC, respectively.

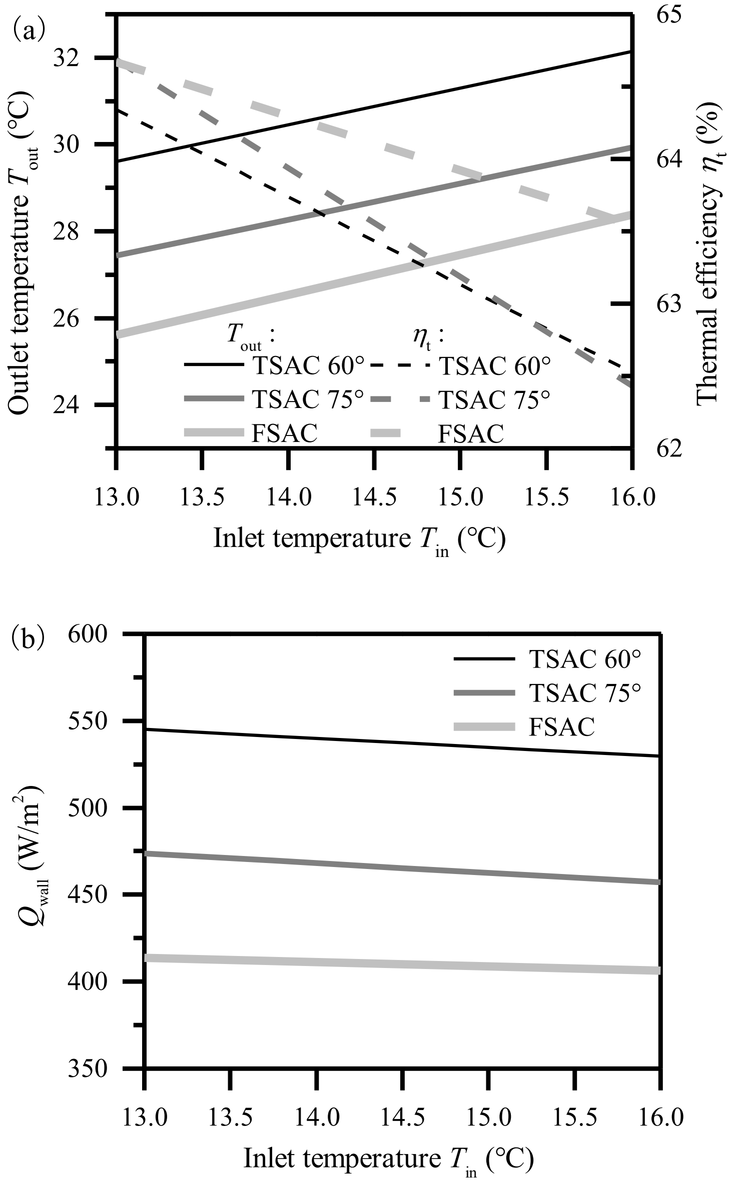

Fig. 6. The effect of air inlet temperature on (a) outlet temperature and thermal efficiency, and (b) heat collecting power of per unit south wall covered area.

Fig. 7a and b show the effect of the flow rate on the performances of the three collectors. With the increase of the flow rate the outlet air temperature decreases, but the convective heat transfer coefficient increases. The thermal efficiencies of the TSAC 75° and FSAC increase slightly, caused by a compromising consequence of the decrease in outlet temperature and increase in transfer coefficient. Whereas the TSAC 60° has a larger cross-sectional area, and a smaller flow velocity and convective heat transfer coefficient, therefore, the thermal efficiency decreases. With the flow rate increasing from 140 to 248 m^3/h, the average outlet temperature of the TSAC 60° is 1.3 and 2.6 ℃ higher than those of the TSAC 75° and FSAC. The CPUWA is linearly related to the thermal efficiency. Considering the thermal comfort, the outlet temperature should not be too low. Assume the outlet temperature is 26 ℃, the corresponding CPUWA of the TSAC 60° is 53.3 and 107.2 W/m^2 higher than those of the TSAC 75° and FSAC, respectively.

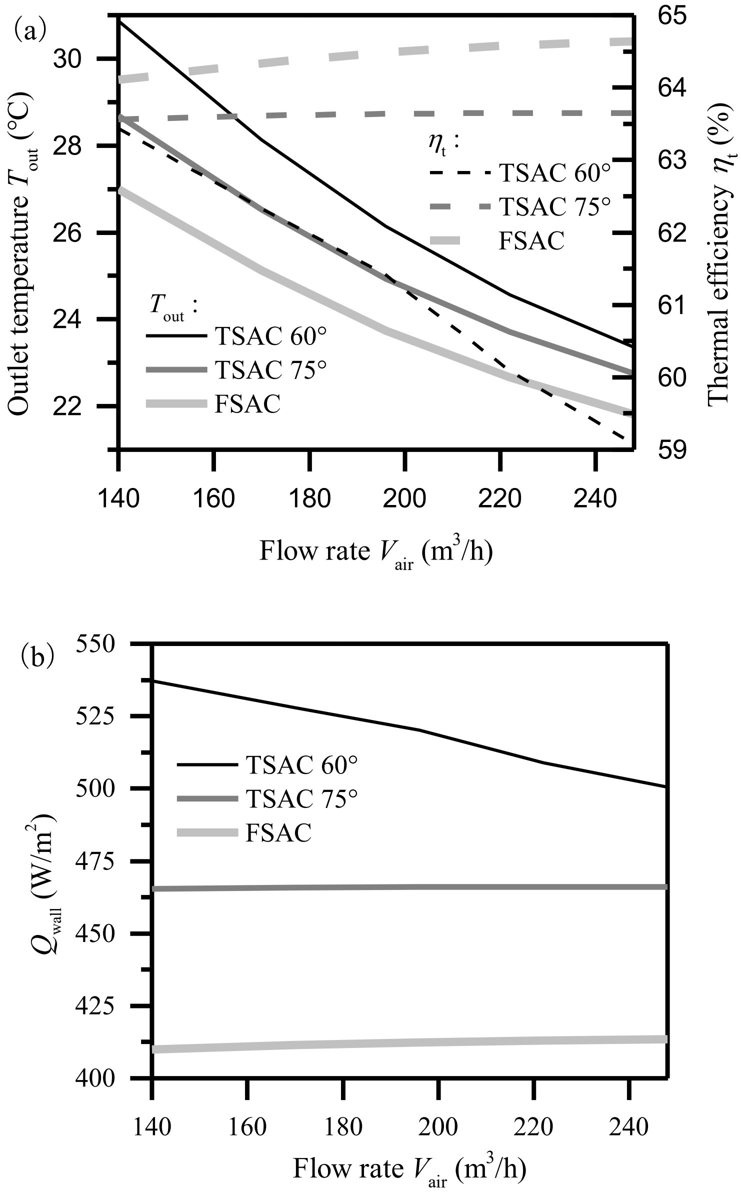

Fig. 7. The effect of flow rate on (a) outlet temperature and thermal efficiency, and (b) heat collecting power of per unit south wall covered area.

4.2 Effects of environmental parameters

The effects of environmental temperature on the performance of the three collectors are illustrated in Fig. 8. The environmental temperature is linearly related to the outlet temperature and thermal efficiency. With the increase of environmental temperature, the heat loss through the transparent cover plate decreases. Due to the large area of the transparent cover plate, the TSACs are susceptible to the variation of environmental temperature, hence, the outlet temperature and thermal efficiency increase rapidly. It is noticed that the thermal efficiency increment of the TSAC 75° is larger than that of the TSAC 60°, since the air flow velocity and the convective heat transfer coefficient in the TSAC 75° is larger, which is more susceptible to environmental temperature than that of the TSAC 60°. When the environmental temperature is higher than 2 °C, the thermal efficiency of the TSAC 75° is higher than that of the TSAC 60° and the FSAC. This indicates that for rural areas with higher average winter temperature, a larger inclination angle of the TSAC is applicable.

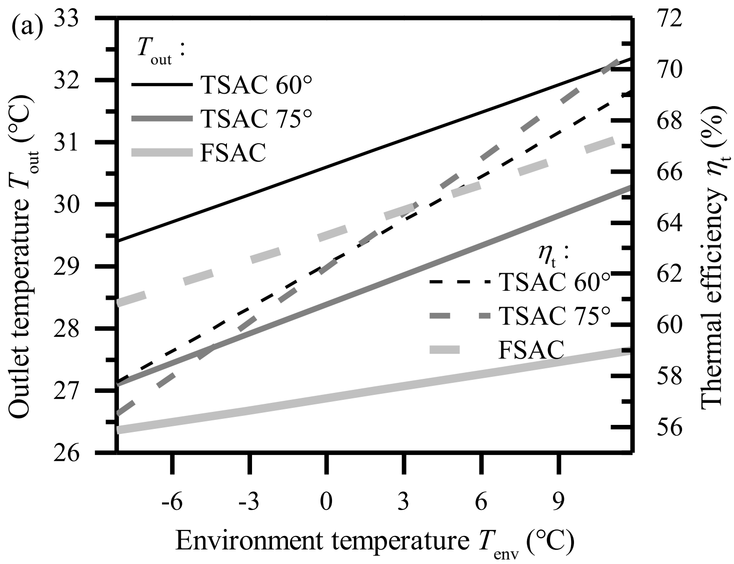

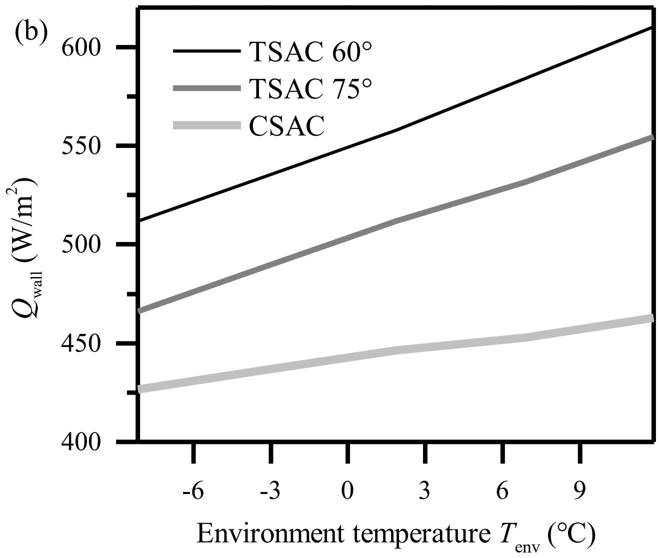

Fig. 8. The effect of environmental temperature on (a) outlet temperature and thermal efficiency, and (b) heat collecting power of per unit south wall covered area.

The effects of the wind speed on the performances of the collectors are shown in Fig. 9. With the increase of the wind speed, the heat loss of the collector increases due to the strengthen of the convective heat transfer between the transparent cover plate and the environment, hence, both of the outlet temperature and thermal efficiency decrease. As the wind speed only reduces the thermal resistance on the outer surface of the transparent cover plate, the change rate of outlet temperature and thermal efficiency decreases when the wind speed is high. The thermal efficiency decrement of the TSAC 75° is larger than that of the TSAC 60°, as it's more sensitive to the wind speed than the TSAC 60°. When the wind speed increases from 0 to 4 m/s, the outlet temperatures of the TSAC 60° and TSAC 75° decrease by 1.4 and 1.9 ℃, respectively. The thermal efficiencies decrease by 5.6% and 8.5%, respectively. The outlet temperature of the FSAC decreases by 0.4 ℃, and the thermal efficiency decreases by 1.9%. Therefore, wind speed has little effect on the thermal performance of the FSAC. For rural areas with high wind speeds, appropriate measures should be taken to reduce TSAC heat loss through the transparent cover plate.

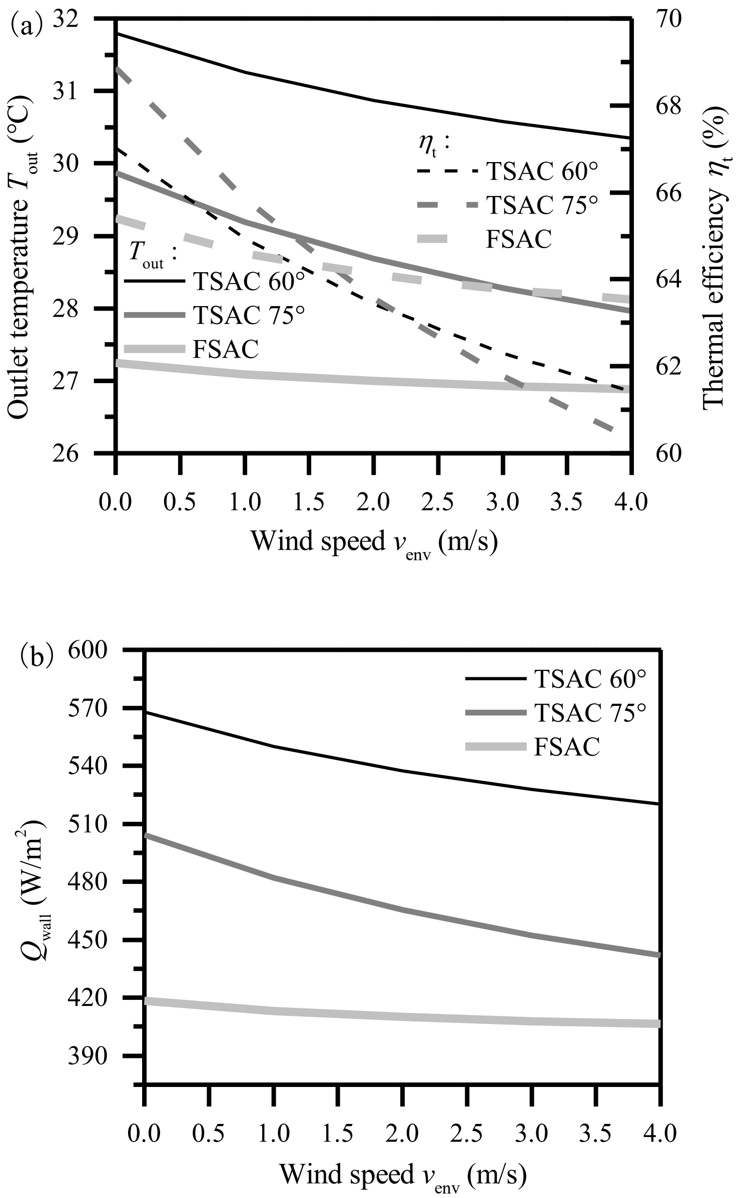

Fig. 9. The effect of wind speed on (a) outlet temperature and thermal efficiency, and (b) heat collecting power of per unit south wall covered area.

The effects of the beam and diffuse solar irradiance on the performances of collectors are illustrated in Fig. 10a, b and c. As shown in Fig. 10a and b, the thermal efficiency and the outlet temperature increase as the beam solar irradiance enhances, which is due to the enhancement of the convective heat transfer between PCA and recirculation air. However, the convective and radiant heat loss of the transparent cover plate to the environment also increases, which leads to the increment of thermal efficiency reduces gradually. The TSAC has a larger area of transparent cover plate, which leads to its susceptibility of outlet temperature and thermal efficiency to the beam solar irradiance, thus the increment is larger. As the beam solar irradiance increases from 400 to 800 W/m^2, the thermal efficiencies of the TSAC 60°, TSAC 75° and FSAC increase by 6.9%, 6.0% and 3%. When the beam solar irradiance is higher than 700 W/m^2, the thermal efficiencies of the two TSACs are higher than that of the FSAC. For rural areas with abundant solar resources, the TSAC is superior. The CPUWA is linearly related to the beam solar irradiance. Within the above range, The CPUWA growth rate of the TSAC 60° is 15.0% and 33.4% higher than that of the TSAC 75° and FSAC, respectively.

The global solar irradiance is composed of beam irradiance and diffuse irradiance. Even on clear days, the diffuse irradiance can account for 10% to 30% (Fan et al., 2019). As shown in Fig. 10c, the effect of the diffuse solar irradiance on the performances of the collectors is similar to that of the beam irradiance. With the diffuse solar irradiance increases from 50 to 250 W/m^2, the outlet temperature and thermal efficiency of the TSAC 60° are increased by 5.1 ℃ and 5.9%, respectively. Hence, when the proportion of the diffuse solar irradiance is high, the effect of diffuse irradiance on the thermal performance of the collector should be considered, especially for the TSAC with a large transparent cover plate area.

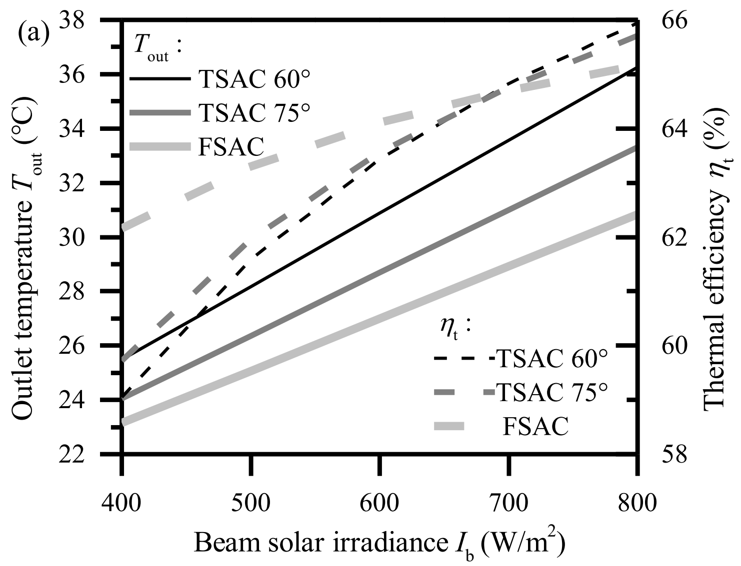
(a)
T_{out} :
TSAC 60°
TSAC 75°
FSAC
η_t :
TSAC 60°
TSAC 75°
FSAC
Outlet temperature T_{out} (°C)
Thermal efficiency η_t (%)
Beam solar irradiance I_b (W/m^2)
22
24
26
28
30
32
34
36
38
58
60
62
64
66
400
500
600
700
800

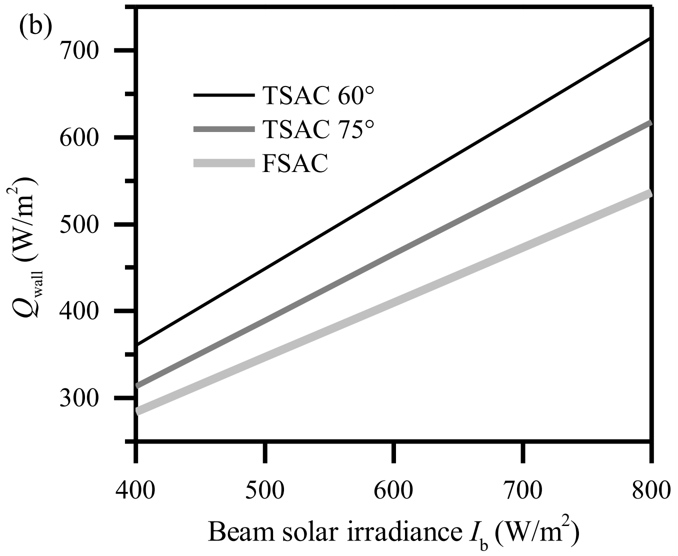
(b)
TSAC 60°
TSAC 75°
FSAC
Q_{wall} (W/m^2)
Beam solar irradiance I_b (W/m^2)
300
400
500
600
700
400
500
600
700
800

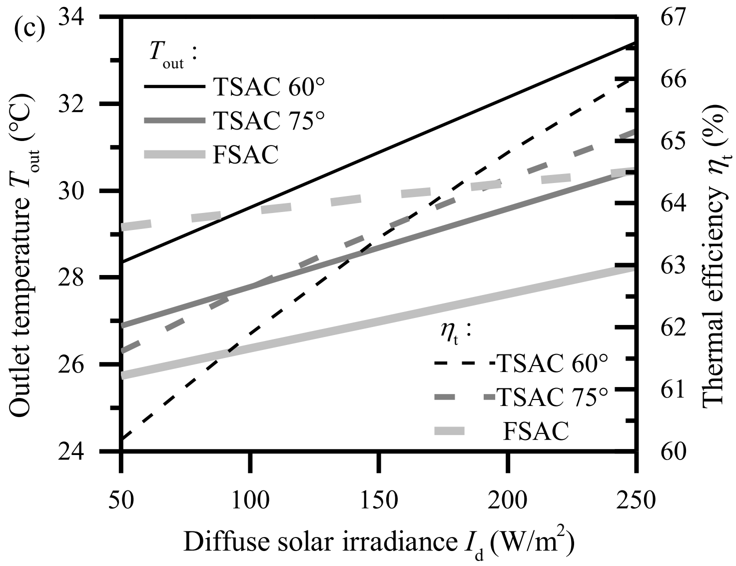

Fig. 10. The effect of beam (a) (b) and diffuse (c) solar irradiance on outlet temperature, thermal efficiency, and heat collecting power of per unit south wall covered area.

The meteorological parameters of January 15 in a typical year of Tianjin, China (39.98 °N, 117.38 °E) were adopted for performance analysis of the collectors, as shown in Fig. 11a. The maximum global solar irradiance is 663 W/m^2, the wind speed fluctuates between 0 ~ 3 m/s, and the environmental temperature is between -3.3 ~ 0.3 ℃. As is shown in Fig.12b, under the effect of solar irradiance, the outlet temperature and thermal efficiency fluctuate greatly at 11:50 and reach the maximum value at 12:10. From 10:00 to 15:30, the average outlet temperature of the TSAC 60°, TSAC 75° and FSAC are 23.0, 22.5 and 22.2 ℃, respectively. The outlet temperature of the FSAC is slightly higher than that of the TSAC 60° and TSAC 75° before 10:30 and after 14:30, but the TSAC 60° is the highest in other periods. The thermal efficiency of the FSAC is higher than TSAC, due to the lower solar irradiance during the period. The thermal efficiency of the FSAC has a small change, as the FSAC has a small area of transparent cover plate, hence it is less affected by the wind speed and environmental temperature. As shown in Fig.12c, the average CPUWA of the TSAC 60°, TSAC 75° and FSAC are 267.1, 249.8 and 241.9 W/m^2, respectively, and the maximum values are 416.6, 380.4 and 341.9 W/m^2 at 12:00, respectively.

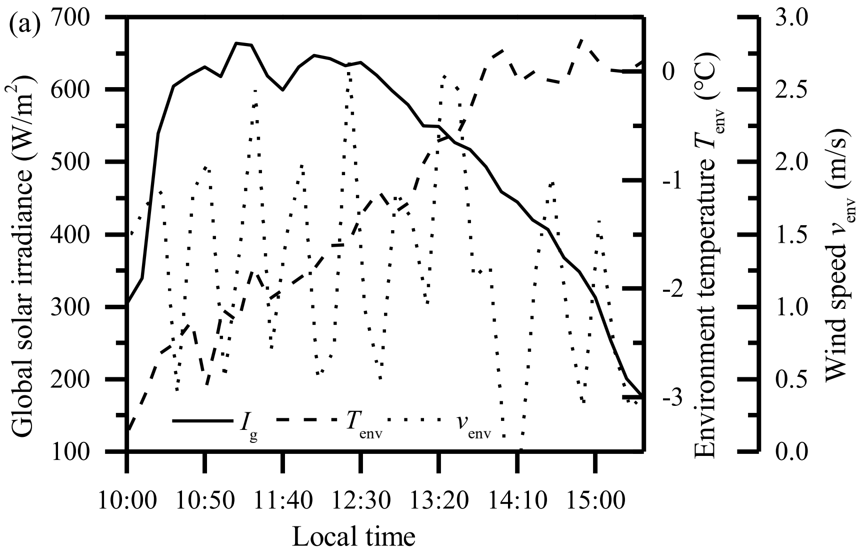

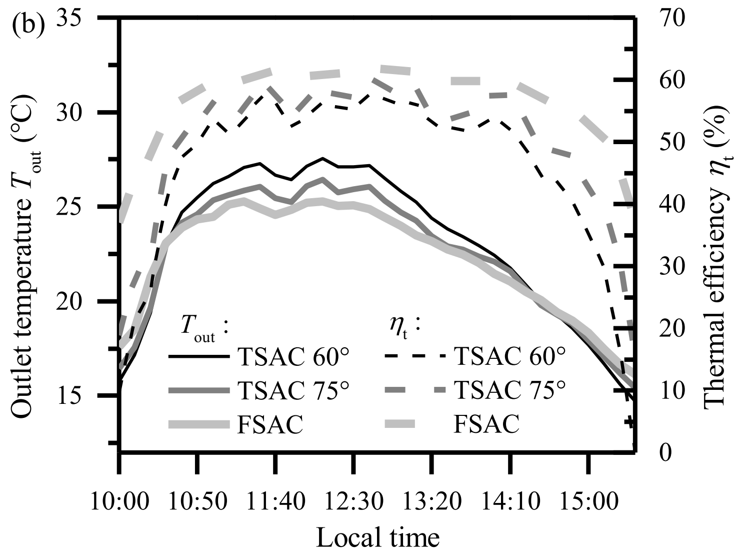

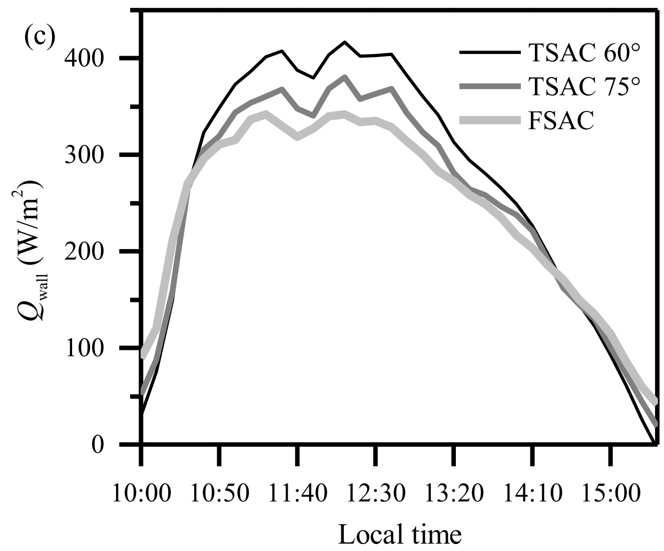

Fig. 11. The (b) outlet temperature and thermal efficiency, and (c) heat collecting power of per unit south wall covered area on (a) actual operating conditions.

4.3 Heat collecting capacity of heating period

Monthly heat collecting capacities of the collectors during the heating period are show in Fig 12. The heat collection capacity of the TSAC 60° is the largest. In December and January, the heat collection capacity of the TSAC 75° is slightly lower than that of the FSAC, due to the low environmental temperature and solar altitude. The heat collecting capacities of the TSAC 60°, TSAC 75° and FSAC are 1425.6, 1229.6 and 1116.9 MJ, respectively. The heat collection capacity of the TSAC 60° is 14.8% and 24.3% higher than that of the TSAC 75° and FSAC, respectively. Assuming the life cycle of the collectors to be 10 years (Saxena et al., 2020b) and the calorific value of standard coal is 29.271MJ/kg, the standard coal savings of the TSAC 60°, TSAC 75° and FSAC are 487.0, 420.1 and 381.6 kg, and the CO_2 emission can be reduced by 1214.3, 1047.2 and 951.4 kg, respectively, and the TSAC has clear advantage for reducing CO2 emission.

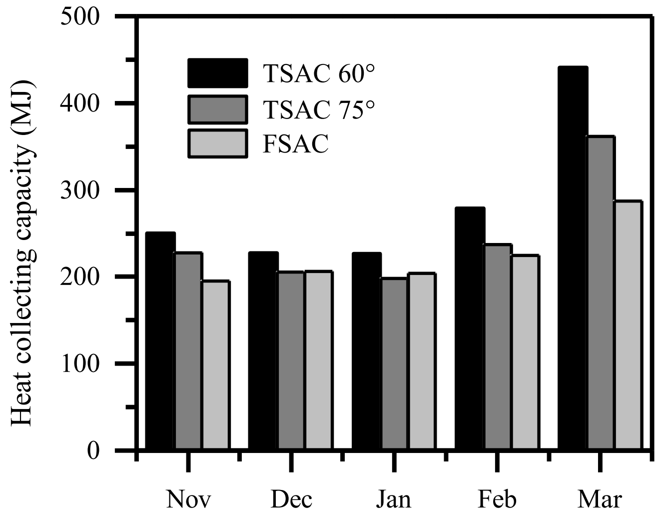

Fig. 12. Comparison of heat collecting capacity in heating period.

In addition, the TSAC is more economical than FSAC. The Annual cost (*AC*) of the TSAC 60° and FSAC are calculated with the methodology introduced by Saxena et al. (2020b). The economic analyses are shown in Table 4. The initial capital investment of the FSAC is \$77, while the TSAC 60° is slightly higher than the FSAC, as it requires more materials. The annual heat collecting capacity of the TSAC 60° is 1425.6 MJ, equivalent to saving 462 kWh electric energy. Considering that the electricity price in China is \$0.11/kWh (Wu et al., 2020), the interest rate (i) is 0.05 and the life cycle of collectors (n) is 10 years. The TSAC 60° can save \$32.8 after annual cost is removed, and saves \$9.10 more than FSAC during a heating period.

$$\begin{aligned} AC &= ACC + AMC - ASV \\ &= \frac{i(i+1)^n}{(i+1)^n-1} \times CI + \frac{i(i+1)^n}{(i+1)^n-1} \times 10\% CI - \frac{i}{(i+1)^n-1} \times 10\% CI \end{aligned} \tag{16}$$

Table 4 Economic analyses of TSAC 60° and FSAC.

Parameters	TSAC 60°	FSAC

Initial capital investment (*CI*)	\$80	\$77
Amount of annual energy saving	396 kWh	310 kWh
Cost of annual energy saving	\$43.56	\$34.10
Annual cost (*AC*)	\$10.76	\$10.36
Annual capital cost (*ACC*)	\$10.36	\$9.97
Annual maintenance cost (*AMC*)	\$1.04	\$1.00
Annual salvage value (*ASV*)	\$0.64	\$0.61
Net annual saving	\$32.80	\$23.74

4.4 Solar fraction for rural residence

The solar fraction of the collectors and heat loss for rural residence during the heating period are shown in Fig. 13. The design indoor temperature of the rural residence is 14.5 °C. The residence area in the case study is 22 m^2, which is 15 times of the collector south wall covered area. In December and January, the environmental temperature and solar irradiance are low, but the heat loss of rural residence is large, which leads to the low solar fraction. After January, the solar fraction of the TSAC is significantly higher than that of the FSAC, which contributes to the increase of the environmental temperature and solar altitude. Thermal efficiency of the TSAC is susceptible to the environmental temperature, and the tilted transparent cover plate can receive more solar irradiance at a large solar altitude. During the whole heating period, the average solar fraction of the TSAC 60°, TSAC 75° and FSAC are 43.5%, 39.3% and 33.6%, respectively. The solar fraction of the TSAC 60° is 6% and 11.7% higher than that of the TSAC 75° and FSAC.

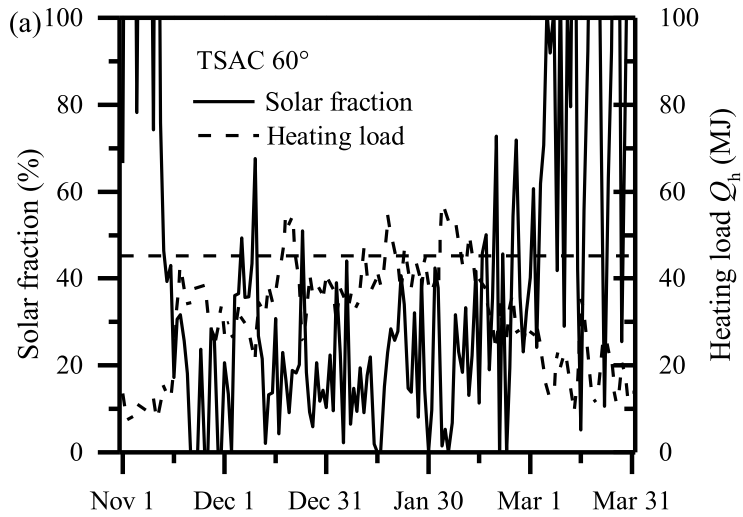
(a)
TSAC 60°
Solar fraction
Heating load
Solar fraction (%)
Heating load Q_h (MJ)
0
20
40
60
80
100
Nov 1
Dec 1
Dec 31
Jan 30
Mar 1
Mar 31

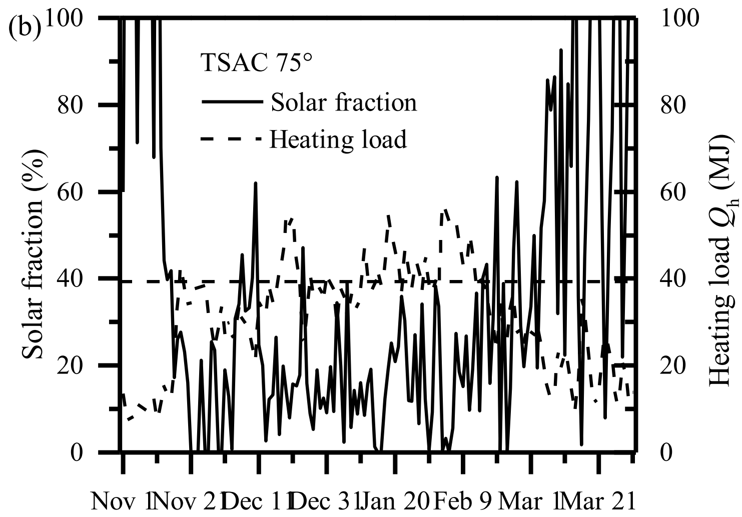
(b)
TSAC 75°
Solar fraction
Heating load
Solar fraction (%)
Heating load Q_h (MJ)
0
20
40
60
80
100
Nov 1
Nov 2
Dec 1
Dec 3
Jan 20
Feb 9
Mar 1
Mar 21

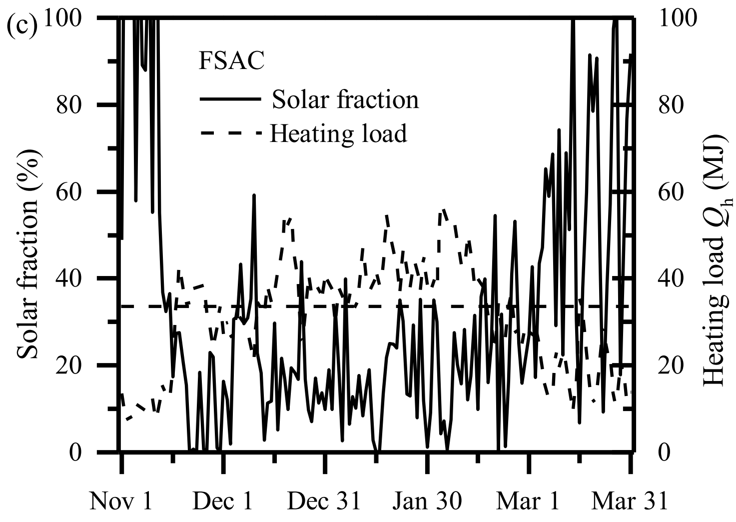

Fig. 13. The solar fractions and heat loss of (a) TSAC 60°, (b) TSAC 75° and (c) FSAC for rural residence.

The main factors affecting the solar fraction include the indoor design temperature and residence area. Fig. 14 depicts the effects of the indoor design temperature, and the ratio of the residence area to collector south wall covered area on the average solar fraction of heating period. As shown in Fig. 14a, with the rise of indoor design temperature, the solar fraction decreases. This is because of that the rise of building heat losses, and the decrease of collector efficiency caused by inlet air temperature. When the indoor design temperature is 13 °C, the maximum solar fractions of the TSAC 60°, TSAC 75° and FSAC are 56.7%, 49.5% and 41.4%. As shown in Fig. 15b, with the rise of residence area, the solar fraction decreases due to the rise of building heat losses. If the TSAC 60° serves as an auxiliary heating equipment and the heat collecting capacity reaches 50% of the rural residence heat loss, the heating area of the rural residence should not exceed 15 times of the TSAC 60° south wall covered area.

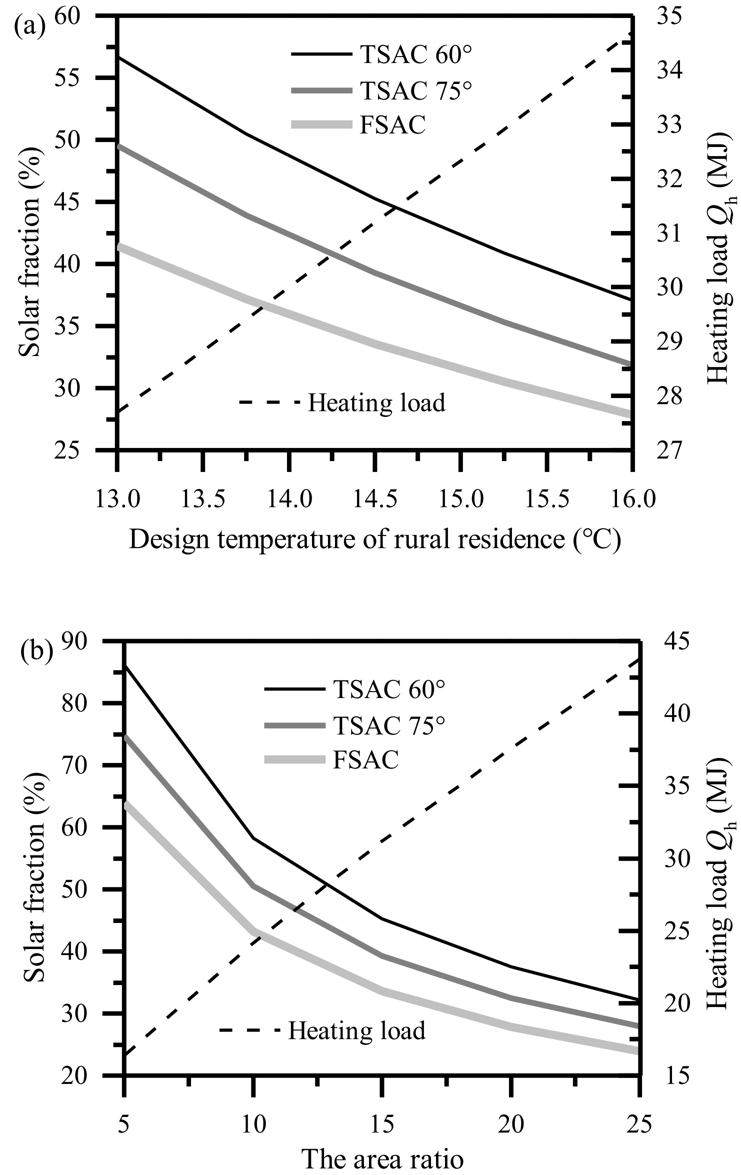

Fig. 14. The effects of the (a) indoor design temperature, and (b) the ratio of the residence area to collector south wall covered area on the solar fraction.

5. Conclusions

To improve the CPUWA of the SAC, a novel TSAC with a tilted transparent cover plate is designed, which can receive more solar irradiance under the same south wall covered area. The mathematical model of the TSAC is developed and verified by experimental results. The thermal efficiency, CPUWA, heat collecting capacity and solar fraction of the TSAC 60° TSAC 75° and FSAC are compared under different operational and environmental conditions. The main conclusions are drawn as follows:

(1) The maximum relative errors of the simulated and tested outlet temperature and net heat gain are 6.0 % and 10.8%, respectively. The tested and predicted results exhibited good agreements, which indicates that the proposed mathematical model was reliable.

(2) Under different operational and environmental conditions, the average outlet temperature and CPUWA of the TSAC 60° are higher than those of the TSAC 75° and FSAC. The heat collection capacity of the TSAC 60° is 14.8% and 24.3% higher than that of the TSAC 75° and FSAC.

(3) The TSAC is more susceptible to the variation of environmental conditions, the thermal efficiency of the TSAC is higher than that of the FSAC, when the environmental temperature and irradiance are higher, and the wind speed is lower.

(4) During the heating period, the solar fraction of the TSAC 60° is 6% and 11.7% higher than that of the TSAC 75° and FSAC.

This study shows significance in increasing heat collecting power of solar air collector under per unit south wall covered area, and the results contribute to promoting the application of solar air collector in the auxiliary heating of rural residence. In the near future, the absorber structure and the optical properties of the triangular solar air collector should be further studied, and flat plate solar air collector of equal aperture area installed at the same tilt as the triangular solar air collector are intended to be compared.

Acknowledgement

This work was supported by the National Key R&D Program of China (No. 2020YFD1100304-06).

References

Acuna A., Lara F., Rosales P., Suastegui J., Velazquez N., Ruelas A., 2017. Impact of a vertical geothermal heat exchanger on the solar fraction of a solar cooling system. International Journal of Refrigeration 76, 63-72.

Badescu V., Soriga I., Ciocanea A., 2019. Solar air collector performance in transient operation under radiative regimes with different levels of stability. Solar Energy 177, 200-212.

Demou A.D., Grigoriadis D.G.E., 2018. 1D model for the energy yield calculation of natural convection solar air collectors. Renewable Energy 119, 649-661.

Deng M., Ma R., Lu F., Nie Y., Li P., Ding X., Yuan Y., Shan M., Yang X., 2021. Techno-economic performances of clean heating solutions to replace raw coal for heating in Northern rural China. Energy & Buildings 240, 110881.

Fan M., You S., Gao X., Zhang H., Li B., Zheng W., Sun L., Zhou T., 2019. A comparative study on the performance of liquid flat-plate solar collector with a new V-corrugated absorber. Energy Conversion and Management 184, 235-248.

Fan M., Zheng W., You S., Zhang H., Jiang Y., Wu Z., 2020. Comparison of different dynamic thermal performance prediction models for the flat-plate solar collector with a new V-corrugated absorber. Solar Energy 204, 406-418.

Gao M., Wang D., Liu Y., Wang Y., Zhou Y., 2020. A study on thermal performance of a novel glazed transpired solar collector with perforating corrugated plate. Journal of Cleaner Production 257, 120443.

Hu J., Liu K., Ma L., Sun X., 2018. Parameter optimization of solar air collectors with holes on baffle and analysis of flow and heat transfer characteristics. Solar Energy 174, 878-887.

Kashif A., Ali M., Sheikh N. A., Vukovic V., Shehryar M., 2020. Experimental analysis of a solar assisted desiccant-based space heating and humidification system for cold and dry climates. Applied Thermal Engineering 175, 113-126.

Kenna J.P., 1983. The thermal trap solar collector. Solar Energy 31, 335-338.

Kumar A., Bhagoria J.L., Sarviya R.M., 2009. Heat transfer and friction correlations for artificially roughened solar air heater duct with discrete W-shaped ribs. Energy Conversion and Management 50, 2106-2117.

Kumar N., Kumar A., Maithani R., 2020. Development of new correlations for heat transfer and pressure loss due to internal conical ring obstacles in an impinging jet solar air heater passage. Thermal Science and Engineering Progress 17, 100493.

Kumar R., Goel V., Singh P., Saxena A., Kashyap A S., Rai A., 2019. Performance evaluation and optimization of solar assisted air heater with discrete multiple arc shaped ribs. Journal of Energy Storage 26, 100978.

Leon M.A., Kumar S., 2007. Mathematical modeling and thermal performance analysis of unglazed transpired solar collectors. Solar energy 81, 62-75.

Li X., Li C., Li B., 2016. Net heat gain assessment on a glazed transpired solar air collector with slit-like perforations. Applied Thermal Engineering 99, 1-10.

Li S., Wang H., Meng X., Wei X., 2017. Comparative study on the performance of a new solar air collector with different surface shapes. Applied Thermal Engineering 114, 639-644.

Liu W., Ren H., Ma Z., 2020. Mathematical modelling and experimental investigation of solar air collectors with corrugated absorbers. Renewable Energy 145, 164-179.

Razak A.A., Majid Z.A.A., Basrawi F., Sharol A.F., Ruslan M.H., Sopian K., 2019. A performance and technoeconomic study of different geometrical designs of compact single-pass cross-matrix solar air collector with square-tube absorbers. Solar Energy 178, 314-330.

Saxena A., Varun, Ei-Sebaii A.A., 2015. A thermodynamic review of solar air heaters. Renewable and Sustainable Energy Reviews 43, 863-890.

Saxena A., Agarwal N., Cuce E., 2020a. Thermal performance evaluation of a solar air heater integrated with helical tubes carrying phase change material. Journal of Energy Storage 30, 101406.

Saxena A., Verma P., Srivastava G., Kishore N., 2020b. Design and thermal performance evaluation of an air heater with low cost thermal energy storage. Applied Thermal Engineering 167, 114768.

Shetty S P., Madhwesh N., Karanth V., 2021. Numerical analysis of a solar air heater with circular perforated absorber plate. Solar Energy 215, 416-433.

Singh A K., Agarwal N., Saxena A., 2021. Effect of extended geometry filled with and without phase change material on the thermal performance of solar air heater. Journal of Energy Storage 39, 102627.

Singh S., Chaurasiya S.K., Negi B.S., Chander S., Nems M., Negi S., 2020. Utilizing circular jet impingement to enhance thermal performance of solar air heater. Renewable Energy 154, 1327-1345.

Sun C., Liu Y., Duan C., Zheng Y., Chang H., Shu S., 2016. A mathematical model to investigate on the thermal performance of a flat plate solar air collector and its experimental verification. Energy Conversion and Management 115, 43-51.

Tuncer A.D., Sozen A., Khanlari A., Amini A., Sirin C., 2020. Thermal performance analysis of a quadruple-pass solar air collector assisted pilot-scale greenhouse dryer. Solar Energy 203, 304-316.

Van Decker G.W.E., Hollands K.G.T., Brunger A.P., 2001. Heat-exchange relations for unglazed transpired solar collectors with circular holes on a square or triangular pitch. Solar Energy 71, 33-45.

Vengadesan E., Senthil R., 2020. A review on recent developments in thermal performance enhancement methods of flat plate solar air collector. Renewable and Sustainable Energy Reviews 134, 110315.

Watmuff J.H., Charters W.W.S., Proctor D., 1977. Solar and wind induced external coefficients - solar collectors. COMPLES, 2-56.

Wu Z., Sha L., Yang X., Zhang Y., 2020. Performance evaluation and working fluid selection of combined heat pump and power generation system (HP-PGs) using multi-objective optimization. Energy Conversion and Management 221, 113164.

Yu T., Zhao J., Zhou J., Lei B., 2020. Experimental investigation of thermal performance of a heating system combining solar air collector with hollow ventilated interior wall. Renewable Energy 147, 1825-1835.

Zhang T., Tan Y., Zhang X., Li Z., 2016. A glazed transpired solar wall system for improving indoor environment of rural buildings in northeast China. Building and Environment 98, 158-179.

Zheng W., Li B., Zhang H., You S., Li Y., Ye T., 2016. Thermal characteristics of a glazed transpired solar collector with perforating corrugated plate in cold regions. Energy 109, 781-790.

Zhang H., Ma X., You S., Wang Y., Zheng X., Ye T., Zheng W., Wei S., 2018. Mathematical modeling and performance analysis of a solar air collector with slit-perforated corrugated plate. Solar Energy 167, 147-157.

Zhou J., Yu T., Wu H., Lei B., Zheng J., Ji W., 2020. A dynamic model of hollow ventilated interior wall integrated with solar air collector. Applied Thermal Engineering 175, 115380.

Zhang D., Liu C., Zhang J., Jing J., An Z., Wang L., 2021. Thermal economic analysis of a double-channel solar air collector coupled with draught fan: Based on energy grade. Renewable Energy 170, 936-947.

Zhao Y., Meng T., Jing C., Hu J., Qian S., 2020. Experimental and numerical investigation on thermal performance of PV-driven aluminium honeycomb solar air collector. Solar Energy 204, 294-306.